Research article

Preparation of phthalocyanine green nano pigment using supercritical CO_2 gas antisolvent (GAS): experimental and modeling

Nedasadat Saadati Ardestani [a,b,c], Gholamhossein Sodeifian [a,b,c,*], Seyed Ali Sajadian [a,b,c]

[a] Department of Chemical Engineering, Faculty of Engineering, University of Kashan, 87317-53153, Kashan, Iran
[b] Laboratory of Supercriritcal Fluids and Nanotechnology, University of Kashan, 87317-53153, Kashan, Iran
[c] Modeling and Simulation Centre, Faculty of Engineering, University of Kashan, 87317-53153, Kashan, Iran

ARTICLE INFO

ABSTRACT

Phthalocyanine green nano pigment was prepared using supercritical gas antisolvent (GAS) process based on the SC-CO_2 method. Thermodynamic models were developed to study the volume expansion and operating conditions of the GAS process. Peng-Robinson EoS were applied for binary (CO_2 and DMSO) and ternary (CO_2, DMSO, and pigment) systems. A Box–Behnken experimental design was used to optimize the process. Influences of temperature (308, 318 and 328 K), pressure (10, 15 and 20 MPa) and solute concentration (10, 40 and 70 mg/mL) were studied on the particles size and their morphology. The fine particles produced were characterized by SEM, DLS, XRD, FTIR and DSC. Experimental results showed a great reduction in size of pigment particles in comparison to the original particles. The mean particle sizes of nanoparticles were obtained to 27.1 nm after GAS based on SC-CO_2 method.

1. Introduction

Nowadays, supercritical fluids (SCFs) have attracted a great deal of attention in numerous fields, such as solubility of the drug, micronization, and formation of the nanoparticles, extraction, coating, separation and chemical reaction [1, 2, 3, 4, 5, 6, 7, 8]. In most of these cases, SCF serves as a solvent and exhibits high solute diffusion and minor viscosity. Thanks to its advantages such as non-explosiveness, non-flammability, non-combustibility, lack of producing the residual, non-toxicity, recyclability, environmentally friendly characteristics, availability at high purity, low critical pressure and temperature (P_C = 7.38 MPa and T_C = 31.4 °C), and ready availability at low cost of supercritical carbon dioxide (SC-CO_2), SC-CO_2 is now a highly popular SCF [9, 10, 11, 12, 13, 14, 15].

Nano-sized particles can be obtained by various processes including solid-solid, liquid-solid, or gas-solid transitions. Physical and chemical vapor deposition, colloidal chemistry methods, mechanical (milling-grinding), sol–gel, hydrothermal, biological/biomimetic as well as ultrasound and microwave techniques can be mentioned as some of the conventional methods used for production of the nanoparticles [16]. In the traditional technologies for production of the nanoparticles, there are many problems, such as degradation in the structure of particles due to thermal or mechanical stresses. The presence of organic solvents or other

toxic substances in the products and also production of the large particles with inappropriate distribution are among the other problems associated with these processes [17, 18]. Precipitation of the SCF has received a great deal of attention due to its high diffusivity, adjustable solvent power, low viscosity, and ease of mass transfer, and the SCF-based precipitation process (micronization and nanonization) has been more studied. The preparation of small particles (in micro or nano scale) with a tunable particle size distribution (PSD) is one of the prominent issues in the fields of science and industry. Achieving the nanoparticles with the precisely controlled size and shape is the main issue in the size reduction of the solid substances and providing the nano-scaled particles. Size, shape, surface, crystalline structure, and morphology of the particles determine the quality and physical and chemical stability of the final products (i.e., micro and nano particles) [19, 20]. In this regard, SCF-based techniques have been regarded as one of the newly-emerged class of "green" technologies to produce the fine particles. In such procedures, the particle size and PSD are influenced by the operational condition (i.e., pressure, temperature, solute (dye, pigment) concentration, carbon dioxide content, and anti-solvent/co-solvent ratio) [21, 22].

In the SCF-based technique to produce the micro/nano particles, SCFs can be used as an anti-solvent, solvent, and reaction media. The entire range of such processes could be classified in different classes: (1) SCF as a solvent; e.g., rapid expansion of the supercritical solution (RESS) [10,

---

23, 24, 25, 26], rapid expansion of the supercritical solution into liquid solvent (RESOLV) [27], and rapid expansion of the supercritical solution with a nonsolvent (RESS-N) [28,29], (2) SCF as an anti-solvent; e.g., gas anti-solvent (GAS) [30, 31, 32, 33], supercritical anti-solvent (SAS) [24, 34, 35, 36], supercritical assisted atomization (SAA) [37], aerosol solvent extraction system (ASES) [38], solution-enhanced dispersion by the supercritical fluids (SEDS) [39], and particles by the compressed anti-solvent (PCA) [40], (3) SCF as the cosolvents; e.g., particles from the gas-saturated solutions (PGSS) [24, 41, 42], PGSS-drying [43], gas-assisted melting atomization (GAMA), and depressurization of the expanded liquid organic solution (DELOS) [44], and (4) SCF as a nebulization compound; e.g., carbon dioxide-assisted nebulization with a bubble dryer (CAN-BD) [44] and supercritical fluid-assisted atomization (SAA) [16, 45, 46, 47]. Recently, Sodeifian *et al.*, reported the use of a new ultrasonic method combined with RESSAS and RESOLV (US-RESSAS and US-RESOLV) [48, 49].

Supercritical dyeing (SCD) technology and its micro- or nano-sized products have been used to improve the performance of the dyes or pigments and prevent the environmental pollution (water) during the dying process. The main challenge of the pigments is their poor solubility in the water and other matrices. The SCF has been used as an anti-solvent (GAS process) for the compounds with poor solubility in the SC-CO_2 and high polarity (such as different pigments, pharmaceuticals, and temperature-sensitive materials) [50].

As a batch (discontinuous) procedure, GAS exhibits its maximum efficiency in the case of using the SFC-insoluble solid solutes in the highly soluble liquids. In other words, the solute should be carbon dioxide-insoluble; while the organic solvent should exhibit high carbon dioxide solubility at the precipitation temperatures and pressures. The GAS process relies on the solution expansion by the SC-CO_2. In this case, the liquid solvents are not proper for dissolving the solute or occurrence of nucleation. In fact, the liquid phases are employed for dissolving the SC-CO_2 which will abruptly reduce the solvent's solvating power and result in the development of the solid precipitates [17]. Actually, in this process, the solid is solved in the solvent including methanol, ethanol, dimethyl sulfoxide (DMSO), etc. The prepared solution is loaded into the sedimentation cell. After introducing the SC-CO_2 with suitable flow rate into the cell, the solution is expanded. This results in a decrease the liquid solvent power and ultimately, deposition of the dissolved particles in the solution [20]. There are many studies on the production of the nanoparticles by the GAS method in the literature. Muller *et al.* [20], investigated the GAS method for micronization of an organic drug. Bothun *et al.* [51], and Cocero-Ferrero [52] considered the GAS to produce the amorphous polylactic acid particles from the chloroform and to perform the micronization of β-carotene, respectively. The molar volume expansion is a key parameter of the GAS. The knowledge about this parameter contributes to the control of the super saturation and PSD. Also, the lowest relative molar volume expansion is related to the highest available super saturation. Upon addition of an anti-solvent, the volume expansion occurs, which may be attributed to the SCF dissolution in the solvent. This leads to a decrease in the solvent density and power. The volumetric expansion has been calculated using the thermodynamic models [53, 54, 55]. It is worth noting that, during a GAS process, particles may precipitate not necessarily under the optional (arbitrary) operating conditions; in such cases, rather the thermodynamic models should be used to find the suitable conditions for retaining the feasibility of the process in practice. Thermodynamic models relate the phase behavior to the formation and growth of the particles. Additionally, the modeling demonstrates the effect of anti-solvent addition on the mean particle size and PSD of the final products [7, 45, 56]. It should be emphasized that, the knowledge about the dynamics, kinetics, and mechanism of particle formation via the GAS technique may have the important contributions to the control over size ad PSD of the precipitated particles [22, 30, 57].

Thanks to their superior physicochemical properties, phthalocyanines (Pcs), and in particular copper-phthalocyanine (CuPc) are the chemically and thermally stable organic materials that have been extensively studied, both theoretically and experimentally. The behavior of Pcs in the solutions and the structure of their crystals in various forms (e.g., nanoparticles, micro-particles, or films) have attracted a great deal of interest. Commercially known as the Pigment Green7, phthalocyanines green (Pc-G) or copper perchloro phthalocyanine (**CuPhcCl$_{16}$**) is one of the members of Pc class. This synthetic green pigment is indeed a complex consisting of copper (II) and chlorinated Pc [58, 59].

According to the literature review, no research has addressed the production of Pc-G nanoparticles via the GAS process and its thermodynamic modeling. It is noteworthy that, in our previous work, experimental solubility and thermodynamic modeling of the Pc-G in SC-CO_2 was investigated at pressures and temperatures ranging within 10–35 MPa and 308.15–338.15 K, respectively. The mole fraction of the Pc-G dissolved in the SC-CO_2 was obtained in the range of 0.01×10^{-5} to 12.12×10^{-5} [60].

In this study, the feasibility of the GAS process to decrease the particle size of the Pc-G (nano- sized) was evaluated. The parameters influencing the process were studied and optimized by the Box–Behnken design (BBD). BBD is a suitable and up-to-date optimization method classified as a rotatable or nearly rotatable second-order design based on the three-level incomplete factorial designs [61, 62].

GAS process conditions resulting in the optimal Pc-G precipitation were determined by modeling the volume expansion and phase equilibrium (thermodynamic model). In this system, pigment (Pc-G) was considered as the solute while, the DMSO and SC-CO_2 played the role of solvent and anti-solvent, respectively. Procedure parameters, such as pressure, temperature, and solute concentration were investigated and their effect on the particle size and PSD of the produced Pc-G particles was evaluated using the BBD. Various analytical methods (dynamic light scattering (DLS), Fourier transform infrared spectrometry (FTIR), scanning electron microscopy (SEM), X-ray diffraction (XRD), and differential scanning calorimetry (DSC)) were conducted to characterize the specimens (processed particles) using different analyses. Finally, a comparison was made between the processed and unprocessed particles.

2. Experimental section

2.1. Materials

Phthalocyanine green Pc-G, CAS Number (14832-14-5) and Dimethyl sulfoxide (DMSO, CAS Number: 67-68-5) with a purity (GC) of ≥99.0% were supplied from Sigma-Aldrich (USA). High-purity (99.99%) carbon dioxide (CO_2) (CAS Number 124-38-9) was prepared by Fadak Company (Kashan, Iran). All the mentioned substances were applied as-received with no extra further purification. The details of the employed compounds are presented in our previous work [60].

2.1.1. Equipment and process of gas anti-solvent (GAS)

Figure 1 schematically illustrates the setup applied in the GAS batch-fed precipitation procedure. The employed GAS pilot plant included several parts: a CO_2 cylinder (P-1), a metal μm filter (Hylok, 6000 psi) (P-2), a refrigeration unit to provide liquefied CO_2 (P-3), an air compressor (P-5) -equipped high-pressure pump (Haskel pump, MSHP-110) (P-6) for supercritical fluid delivery, a 100-mL precipitation unit (P-8), a system for automation (P-10) which encompasses pressure assessment tools (pressure gauge and digital pressure transmitter (WIKA) and a back-pressure regulator (GO; BP-66)) (P-9), temperature measuring unit (consisting of digital thermometer, temperature indicator), a temperature-tunable oven (Froilabo AE-60, France) combined with Pt 100 temperature sensors (±0.1 K) (P-7), and sintered metal filter along with a polymer filter (PTFE) (P-11) on which the particles were supposed to be precipitated (P-13). The entire fittings and piping process were implemented using 1/8″ stainless steel 316 capable of tolerating high pressure values (up to 45 MPa).

First, solutions of Pc-G in the DMSO were prepared at various concentrations: 10, 40, and 70 mg/mL. Also, the operating temperature
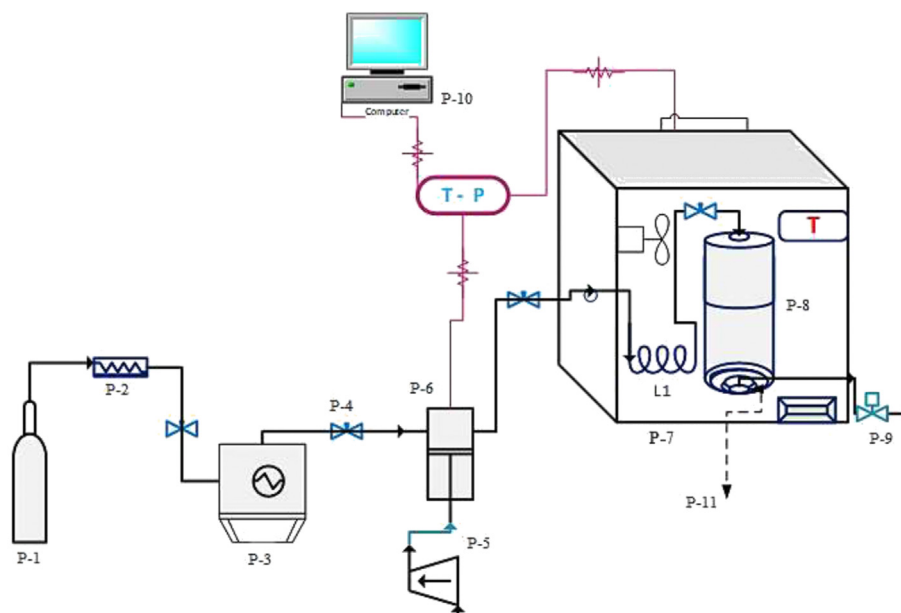
Equipment List		
Designation	Description	Material
P-1	CO$_2$ cylinder	CO$_2$
P-2	Filter	CO$_2$
P-3	Refrigerator unit	CO$_2$
P-4	High pressure valve	
P-5	Air compressor	Air
P-6	High pressure pump	CO$_2$
P-7	Oven	
P-8	Precipitator cell	CO$_2$+ Pc-G+DMSO
P-9	Back pressure	
P-10	Control panel	
P-11	Sintered filter	

Figure 1. Schematic experimental setup employed for nanoparticle production by the GAS process.

(308, 318, and 328 K) and pressure (10, 15, and 20 MPa) were chosen for the experimental data. The operating conditions of the process (temperature and pressure) were selected using the thermodynamic modeling and initial tests (preliminary test) [21, 63, 64]

Then, 2 mL of this solution (Pc-G - solvent) was loaded into the precipitation cell. After passing through a metal μm filter (pore size of 1 μm) used to remove the particle contaminations at the size of μm, the carbon dioxide was introduced into the refrigeration system where it was compressed and converted into the liquefied gas through temperature decline. The liquefied gas pressure was equivalent to the CO$_2$ cylinder pressure (6 MPa) when it left the refrigeration unit. Afterwards, it was charged into a reciprocating pump, in which its pressure was changed to the intended one. The CO$_2$ flow rate was equal to 1 g/min and also, the accuracy of the pressure transmitter and gauge was equal to ±0.1 MPa. For reaching the desired temperature, the precipitation cell was placed inside an oven. The inner diameter and length of precipitation unit were equal to 60 and 120 mm, respectively. SC-CO$_2$ was pressurized and applied from the top of the precipitation cell by stabilizing the operating condition at its set point in the precipitator cell while, the outlet valve on the bottom of the cell was sealed throughout the precipitation stage. After providing the desired pressure in the precipitator, the pump was turned off, the input valve on the bottom of the cell was closed and the precipitator conditions were kept constant for 90 min. Although, the CO$_2$ stream could diffuse and pass the sintered metal and polymer filters placed on the cell bottom, the pigment particle was precipitated on the filters. At last, the Pc-G particles were collected after depressurizing the precipitator.

2.1.2. Experimental design (BBD) for nanoparticle production via GAS

The Box–Behnken experimental design (BBD) was coupled with response surface methodology to assess the input variables and their interactions to determine the optimal response [61, 65]. A 3-factor and 3-level Box–Behnken design was employed to investigate the impact of the procedure factors on the morphology and of size the Pc-G precipitates obtained from the GAS approach. DLS technique was applied to determine the mean particle size (x_{50}). The independent-dependent variables correlation was assessed by fitting the experimental data with the following second-order quadratic polynomial relation [66, 67, 68]:

$$Y = \beta_0 + \beta_1 A_1 + \beta_2 A_2 + \beta_3 A_3 + \beta_{11} A_1^2 + \beta_{22} A_2^2$$
$$+ \beta_{33} A_3^2 + \beta_{12} A_1 A_2 + \beta_{13} A_1 A_3 + \beta_{23} A_2 A_3 \qquad (1)$$

in which, Y shows the process response (output); while $A_1 - A_3$ denote the coded independent parameters. β_0 represents the intercept term; whereas $\beta_1 - \beta_3$ stand for the linear coefficients. β_{12}, β_{13} and β_{23} show the interaction coefficients; β_{11}, β_{22}, and β_{33} represent the quadratic coefficients. The analysis of variance (ANOVA) was also conducted considering R^2, adjusted R^2, predicted R^2 and F-values. Moreover, the experimental data were graphically analyzed using the Design Expert 7.0.0 software. This research employed a quadratic model which included the linear, interactive and quadratic terms.

2.1.3. Particle characterization

The structural, morphological and surface properties of the GAS-produced particles were investigated using Fourier Transform Infrared

Spectrophotometer (FTIR) and Field Emission Scanning Electron Microscope (FESEM; Hitachi, S-4160 FESEM apparatus (20 kV)., Japan). Furthermore, the PSD of the samples was carried out by dynamic light scattering DLS; a NANOPHOX particle sizer (Sympatec GmbH System-Partikel-Technik) equipped with a He–Ne laser (wavelength: 623 nm, power: 10 mW). The thermal stability of the specimens was investigated by differential scanning calorimetry (DSC; 404 F3 Pegasus, Netzsch Co., Germany). In a typical procedure, the temperature of the samples (5 mg/run) were elevated from 303 K (starting temperature) to 503 K (end temperature) with the heating rate of 10 K/min in a standard aluminum pan under an argon flow (20 mL/min). Finally, XRD (XRD; Philips X'pert Pro MPD., Netherland) was utilized at room temperature to examine the crystallinity, phase status and average crystallite size.

3. Thermodynamic framework

For a GAS process, the thermodynamic modeling and phase behavior analysis of the system are essential steps for the evaluation of the process feasibility. For this purpose, volume expansion and phase equilibrium should be investigated by thermodynamic models prior to the experimental steps. To model the GAS process, all phases were assumed to exhibit the same pressure and temperature. Additionally, due to the low volume of the precipitator and mixing of the liquid and gas phases, mass transfer resistance was assumed to be negligible [7, 22, 30].

3.1. Peng-Robinson equation of state (EoS)

The Peng–Robinson equation of state has the following form [69]:

$$P = \frac{RT}{v-b} - \frac{a(T)}{v(v+b)+b(v-b)} \tag{2}$$

In the above equation, absolute pressure (MPa) and temperature (K) are represented by P and T, respectively. v denotes the molar volume (cm^3/mol) while R shows the global gas constant (8.314 J.mol/K). a and b parameters are related to the critical and physical features of the pure components with interaction parameters. For a system composed of only a single compound, a and b are constants which could be determined by:

$$a(T) = \frac{0.45724\,R^2\,T_c^2}{P_c} \times \alpha\,(T_{r,\,\omega}) \tag{3}$$

$$\alpha(T_{r,\,\omega}) = \left[1 + k\left(1 - T_r^{0.5}\right)\right]^2 \tag{4}$$

$$k = 0.37464 + 1.54226\,\omega - 0.26992\,\omega^2 \tag{5}$$

$$b = \frac{0.07780\,R\,T_c}{P_c} \tag{6}$$

In which P_c and T_c stand for the critical pressure (MPa) and temperature (K), respectively. ω represents the acentric factor of the compounds. The reduced temperature is also shown by T_r (where $T_r = T/T_c$). Since no information was found regarding the critical and physical properties of Pc-G, parameters such as the acentric factor, critical pressure and critical temperature as well as the normal boiling point (T_b) were estimated using the group contribution method [70]. Additionally, in a solute-CO_2 system, the a and b parameters desirable for the Peng-Robinson EoS could be described by a two-parameter van der Waals (vdW) mixing rule:

$$a_m = \sum_j y_i y_j\,\sqrt{a_i a_j}\left(1 - k_{ij}\right) \tag{7}$$

$$b_m = \sum_j y_i y_j\,\frac{(b_i + b_j)}{2}\left(1 - l_{ij}\right) \tag{8}$$

l_{ij} and k_{ij} are binary interaction parameters whose optimum values can be obtained by the genetic algorithm (GA).

The equilibrium compositions were assessed on the basis of the PR-EoS using below equation:

$$\sum \phi_i^l - \phi_i^v = 0 \tag{9}$$

3.2. Vapor-liquid-solid equilibrium calculation

$$\ln\frac{\phi_i}{x_i P} = -\frac{A}{2\sqrt{2}B}\left(\frac{2\sum x_j a_{ji}}{a_m} - \frac{b_i}{b_m}\right)\ln\left(\frac{Z+2.414B}{Z-0.414B}\right) - \ln(Z-B)$$
$$+ \frac{b_i}{b_m}(Z-1) \tag{10}$$

With

$$Z = \frac{PV}{RT} \quad A = \frac{Pa_m}{R^2 T^2} \quad B = \frac{b_m P}{RT} \tag{11}$$

The proposed system involves three equilibrated phases (vapor, liquid, and solid (VLS)). The equilibrium condition of the mentioned system includes [7, 53, 55]:

$$\frac{\phi_1^l}{\phi_1^v}x_1 - y_1 = 0 \tag{12}$$

$$\frac{\phi_2^l}{\phi_2^v}x_2 - y_2 = 0 \tag{13}$$

$$\frac{\phi_3^l}{\phi_3^v}x_3 - y_3 = 0 \tag{14}$$

Eqs. (12) and (13) are the equilibrium condition for liquid–vapor equilibrium of binary system. Eqs. (12), (13), and (14) are three equilibrium condition for liquid–vapor equilibrium of ternary system. In Eq. (15) it is supposed that the solid phase is pure solute in the solid liquid equilibrium.

$$\frac{\phi_3^s}{\phi_3^l} - x_3 = 0 \tag{15}$$

In Eq. (15), ϕ_3^s is the fugacity coefficient of solute in solid phase. The following constraints for two fluid phases (liquid and vapor) were used.

$$\sum_{i=1}^{3} x_i - 1 = 0 \tag{16}$$

$$\sum_{i=1}^{3} y_i - 1 = 0 \tag{17}$$

The PR EoS can be employed to model the liquids and vapors. Therefore, the solid phase fugacity coefficient was separately proposed. Below equation can be used for ϕ_3^s calculation [7, 55]:

$$\ln \phi_3^s = \ln \phi_3^{l,pure} + \frac{\Delta H_{tp}}{R}\left(\frac{1}{T_{tp}} - \frac{1}{T}\right) + \frac{v_{tp}}{RT}\left(P - P_{tp}\right). \tag{18}$$

In the above relation, $\phi_3^{l,pure}$ represents the fugacity coefficient of the pure solute present in the sub-cooled liquid with the respective temperature and pressure of T and P. Calculation of the fugacity coefficient requires information on the triple point fusion heat (ΔH_{tp}), temperature (T_{tp} often approximated to the melting point) and pressure (P_{tp}) as well as the solute molar volume at the triple point (v_{tp}).

3.3. Molar volume expansion

Defined by de la Fuente Badilla *et al.*, the relative molar volume change can be obtained by [53]:

$$\frac{\Delta v}{v} = \frac{v(T, P, x1) - v_0(T, P_0)}{v_0(T, P_0, x1)}. \tag{19}$$

where, $v(T, P, x1)$ indicates the molar volume of the liquid phase as a function of the system temperature and pressure, x_1 represents the equilibrium liquid-dissolved CO_2 mole fraction and $v_0(T, P_0, x1)$ stands for the solvent molar volume at the system temperature and the reference pressure (in this work, $P_0 = 1.01325$ bar).

Table 1. Parameters and their levels for the purpose of Box–Behnken experimental design.

Parameters	Level 1	Level 2	Level 3
Pressure (MPa); A_1	10	15	20
Temperature (K); A_2	308	318	328
Solute concentration (mg/mL); A_3	10	40	70
Solvent	DMSO		

4. Results and discussion

4.1. Box–Behnken experimental design and evaluation of the fitted model

Box–Behnken experimental design (BDD) was employed to evaluate the effect of the three process parameters on the size and morphology of the Pc-G precipitates. Various ranges of the independent variables were studied (temperature (A_1; 308, 318, and 328 K), pressure (A_2; 10, 15, and 20 MPa), and initial solute concentration (A_3; 10, 40, and 70 mg/ml)) as listed in Table 1. Based on this design, the average particle size (x_{50}) was considered as an output variable (response) and the required number of experiments was found to be 17. Table 2 shows the empirical results about the decrease in the particle size in different operational conditions. The response relationships with different variables were determined by the BBD approach considering the coded factors using the multiple regression analysis of the experimental results. The relationship between

Table 2. BBD matrix of the GAS processes and quantitative results.

Run	P (A_1) (MPa)	T (A_2) (K)	Solute concentration (A_3) (mg/mL)	Mean particle size (x_{50} -nm)	Predicted value (nm)
1	20.00	328.00	40.00	63.57	66.71
2	15.00	318.00	40.00	116.08	116.07
3	15.00	318.00	40.00	116.08	116.07
4	20.00	308.00	40.00	27.12	28.56
5	15.00	318.00	40.00	116.08	116.07
6	10.00	318.00	70.00	214.87	215.39
7	10.00	318.00	10.00	188.36	192.41
8	10.00	328.00	40.00	233.62	232.17
9	15.00	308.00	10.00	85.17	84.25
10	15.00	328.00	70.00	157.51	158.42
11	20.00	318.00	70.00	67.04	62.98
12	15.00	308.00	70.00	98.22	100.83
13	15.00	318.00	40.00	116.08	116.07
14	20.00	318.00	10.00	41.26	40.73
15	10.00	308.00	40.00	170.34	167.19
16	15.00	328.00	10.00	132.4	129.78
17	15.00	318.00	40.00	116.08	116.07

Table 3. Analysis of variance (ANOVA) for the fitted model to the nanoparticle production process.

Source	Sum of squares	df	Mean square	F- Value	p-value Prob > F	
Model	53161.89	9	5906.88	568.25	<0.0001	significant
A_1-pressure	46238.40	1	46238.40	4448.16	<0.0001	significant
A_2-Temperature	5317.38	1	5317.38	511.54	<0.0001	significant
A_3-Concentration	1022.65	1	1022.65	98.38	<0.0001	significant
A_1*A_2	179.96	1	179.96	17.31	0.0042	significant
A_1*A_3	0.13	1	0.13	0.013	0.9130	
A_2*A_3	36.36	1	36.36	3.50	0.1036	
A_1^2	309.24	1	309.24	29.75	0.0010	significant
A_2^2	4.11	1	4.11	0.39	0.5496	
A_3^2	44.00	1	44.00	4.23	0.0787	
Residual	72.76	7	10.39			
Lack of Fit	72.76	3	24.25			
Pure Error	0.000	4	0.000			
Cor Total	53234.66	16				
Quadratic	Std. Dev.	PRESS	R-Squared	Adj R-Squared	Pred R-Squared	Adeq Precision
	3.22	1164.23	0.9986	0.9969	0.9781	82.341

the response and significant variables can be described using the following second-order quadratic polynomial equation:

$$X_{50} = 116.08 - 76.02A + 25.78B + 11.31C - 6.71AB$$
$$-0.18AC + 3.01BC + 8.57A^2 - 0.99B^2 + 3.23C^2 \qquad (20)$$

Table 3 summarizes the analysis of variance (ANOVA) test results obtained by the Design Expert 7.0.0 software. Accordingly, the higher the *F-value* and the lower the *p-value,* the more significant the corresponding coefficient will be. High *F-values* imply that the regression equations are capable of describing the response variations. Furthermore, *p-values* below 0.05 indicated the statistical significance. As shown in Table 3, the *F-value* (568.25) and *p-value* of the model (<0.0001) clearly confirmed the model significance with a predictability confidence of >95%. Based on the ANOVA results, pressure, temperature, and solute concentration

most significantly influenced the model. R^2 (R-square), adjusted R^2, and predicted R^2 can be employed to check the degree of fit in a quadratic model. Indeed, the larger R^2 and adjusted R^2 indicated the better fitting of the proposed model to the experimental data (i.e., higher input-response correlation). In this study, R^2 (R-square) was equal to 0.9986 while, the adjusted R^2 and predicted R^2 were determined as 0.9969 and 0.9781, respectively. Finally, BBD studies confirmed the acceptable performance of the model with a good reliability. Figure 2(a–c) show the 3D surface diagrams regarding evaluation of the effect of each parameter on the Pc-G pigment nanoparticle size and formation mechanisms. Additionally, Figure 3 presents the diagnostic plots of the model adequacy (model fitting) via the BBD method, which can be applied for comparison of the experimental results with the model-calculated ones. As indicated in Figure 3, the experimental results exhibited a significant
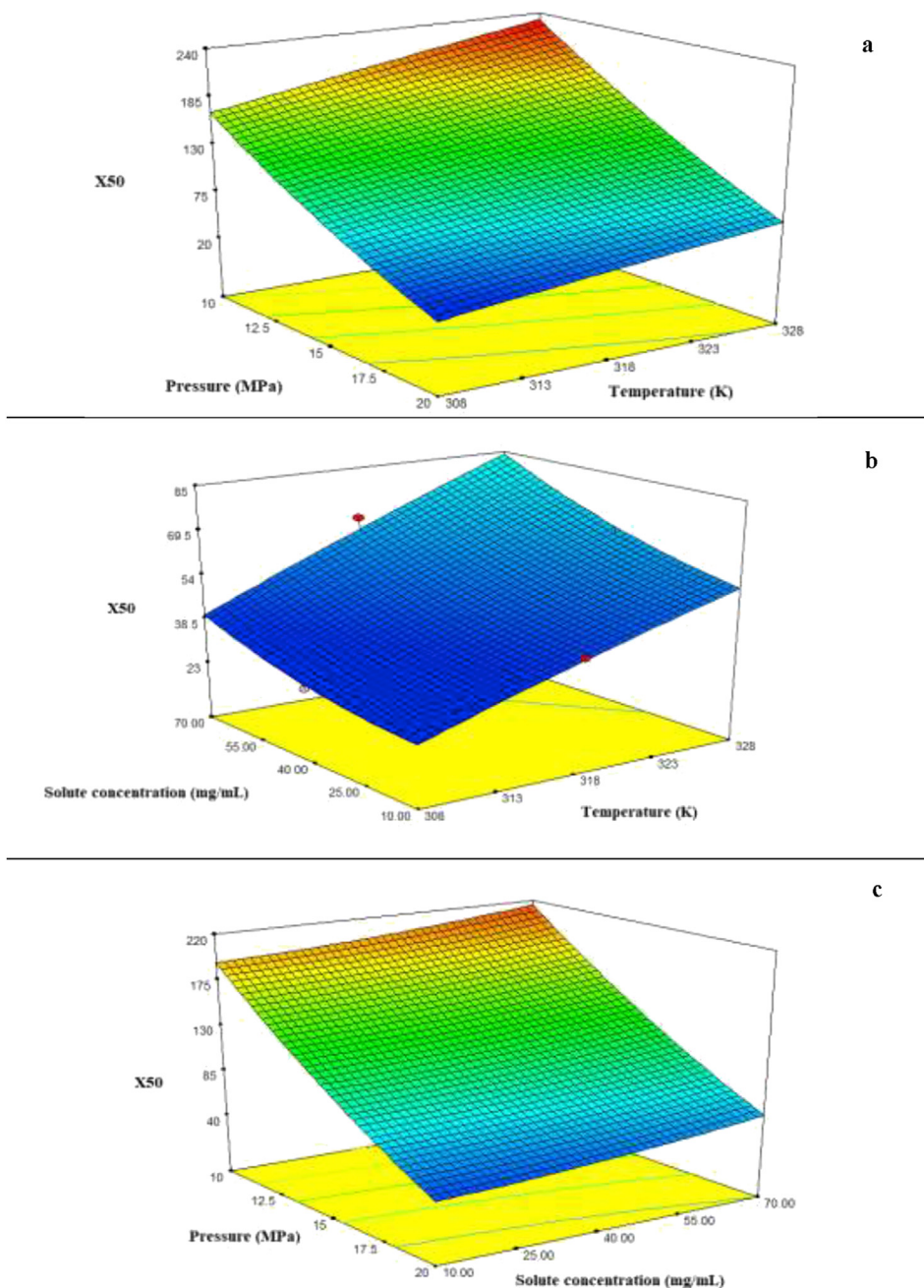
Figure 2. The surface plots representing the impact of (a) temperature and pressure, (b) solute concentration and temperature, and (c) solute concentration and pressure on the particles size.
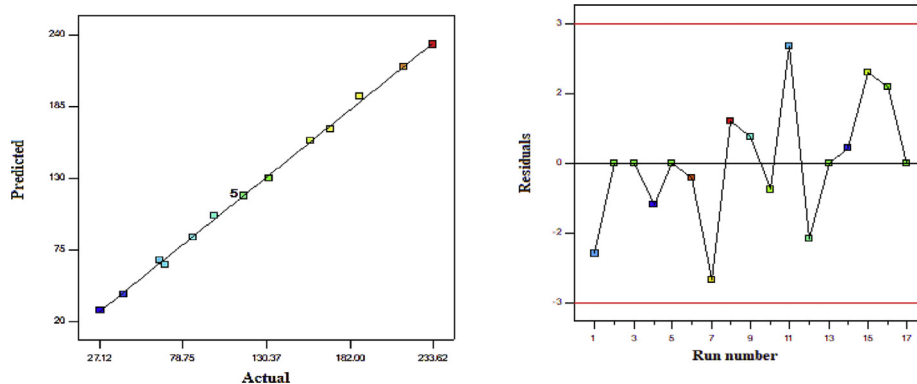
Figure 3. Diagnostic plots for model adequacy (model fitting) from the BBD method.

proximity to the estimated data implying the good fitting to the empirical results. BBD was employed in the Design Expert software to optimize the operational conditions in order to minimize the Pc-G particle size. According to this optimization, a temperature of 308.1 K, the pressure of 19.98 MPa, and the solute (Pc-G) concentration of 33.57 mg/mL will result in an optimal particle size (27.11 nm).

4.2. Effect of the operating parameters

The effect of various parameters was investigated for process optimization.

4.2.1. Temperature

According to Figure 2 and Table 2 (obtained from the Box–Behnken experimental design), enhancement of the process temperature (308, 318, and 328 K) augmented the mean size of the precipitated Pc-G particles. Temperature is important in the GAS process because of its effect on the solubility, super-saturation, and nucleation. The temperature can influence the particle size through nucleation and growth dynamics. Accordingly, a rise in the temperature will enhance the pigment solubility in the organic solvent. Consequently, the augmented pigment-solvent interaction will decrease the pigment solubility in the SC-CO$_2$. Besides, the temperature increase can change the shape of the precipitated particles. The volume expansion decreases by decreasing the solubility and super-saturation, providing a growth in the size of the produced particles. Similar results and trends have also been reported by Muller *et al.* [20], Bakhbakhi *et al.* [71], Chen *et al.* [63], Bakhbakhi *et al.* [22], and Kim *et al.*, [72].

4.2.2. Pressure

Three different pressures (10, 15, and 20 MPa) were evaluated at a constant temperature to assess how the pressure influences the particle size and particle size distribution. As shown in Figure 2 and Table 2 (obtained from the Box–Behnken experimental design), an increase in the process pressure decreased the Pc-G mean particle size. Indeed, the increased pressure might cause a higher volume expansion, favoring the nucleation and hence enhancing its rate. The nucleation mechanism became dominant upon the pressure increase leading to the formation of smaller particles. This might ultimately result in the production of smaller particles of the pigment (Pc-G) [20, 21, 31, 63].

4.2.3. Solute (Pc-G) concentration

Three different solute concentrations (10, 40, and 70 mg solute/mL solution) were investigated to shed some light on its effect on the average particle size and PSD. According to Table 2 and Figure 2, greater Pc-G concentrations resulted in the formation of larger particles, which can be attributed to the process of nucleation and growth. The precipitation will occurr at lower volume expansion by increasing the initial solute concentration, resulting in the longer durations of crystal growth,

ultimately leading to the formation of the larger particles. For greater solute concentrations, the super-saturated profile will rapidly approach the saturation line, causing an initial nucleation explosion, which may superimpose to the secondary nucleation, resulting in the formation of larger particles. Conversely, at lower solute concentrations, solute precipitation will happen at higher volume expansion giving rise to the emergence of smaller particles. Chen *et al.* [63], Esfandiary *et al.* [31], Jafari *et al.* [21], and Bakhbakhi *et al.* [71], also reported similar results concerning the effect of solute concentration on the average particle size and PSD in the GAS process.

4.3. Characterization of the Pc-G

Particle size and morphology are the decisive factors in possible applications of the SC-CO$_2$ in dyeing and dye properties [73, 74]. This highlights the necessity for investigating the structural properties of the nanoparticles. Therefore, GAS-produced Pc-G particles were investigated through various techniques including FTIR, XRD, DSC, FSEM, and DLS.

The unprocessed and GAS-processed specimens were assessed by the FT-IR spectroscopy as depicted in Figure 4 (a, b). Clearly, no shift was observed in the wavenumber; moreover, the peak intensity of the functional groups remained unchanged. The Pcs possessed a highly distinctive spectrum (below 1700 cm^{-1}) encompassing numerous sharp bands as a result of stretching deformation in the aromatic ring carbon-carbon bonds. Also, the peaks at 1630 and 745 cm^{-1} could be attributed to the –C=N and C– Cl bonds, respectively. Several researchers have also reported similar results [58, 75, 76, 77].
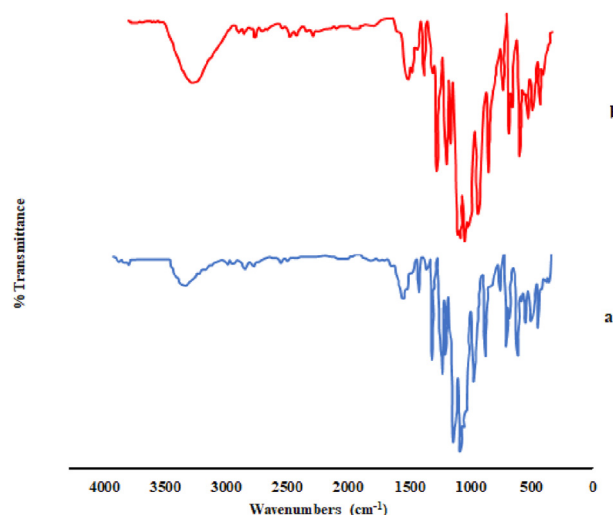

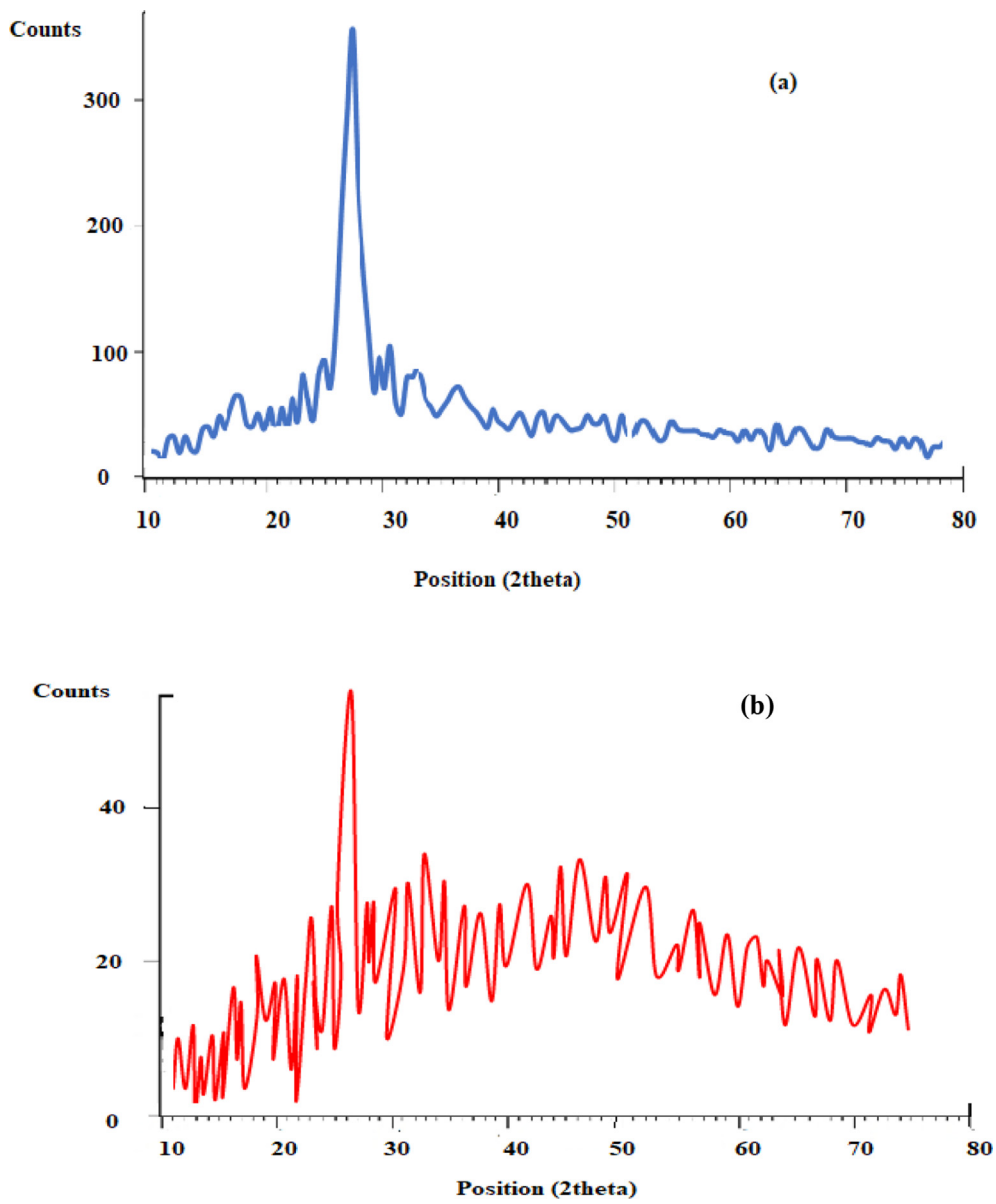**Figure 4.** The FTIR spectra of (a) original and (b) GAS-processed Pc-G particles.

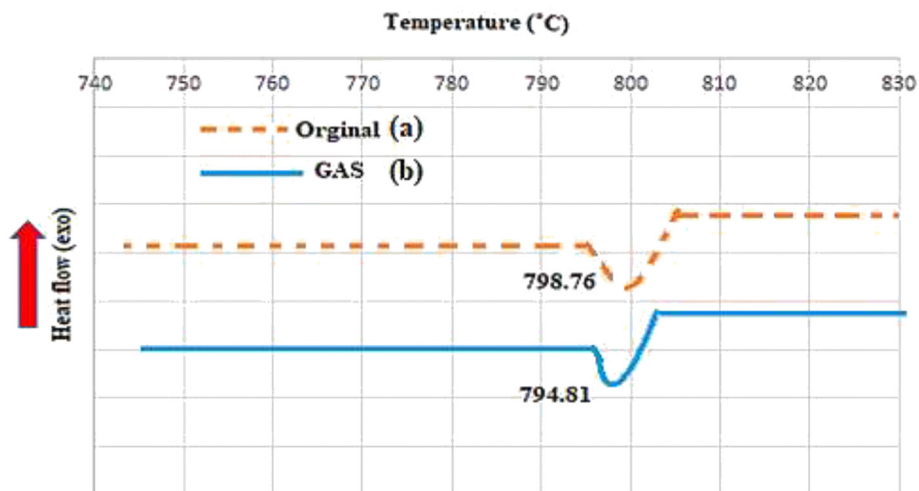Figure 5. XRD patterns of Pc-G before and after the processes: (a) original and (b) GAS-processed.

Figure 6. DSC analysis of Pc-G before and after the process: (a) original and (b) GAS-processed.
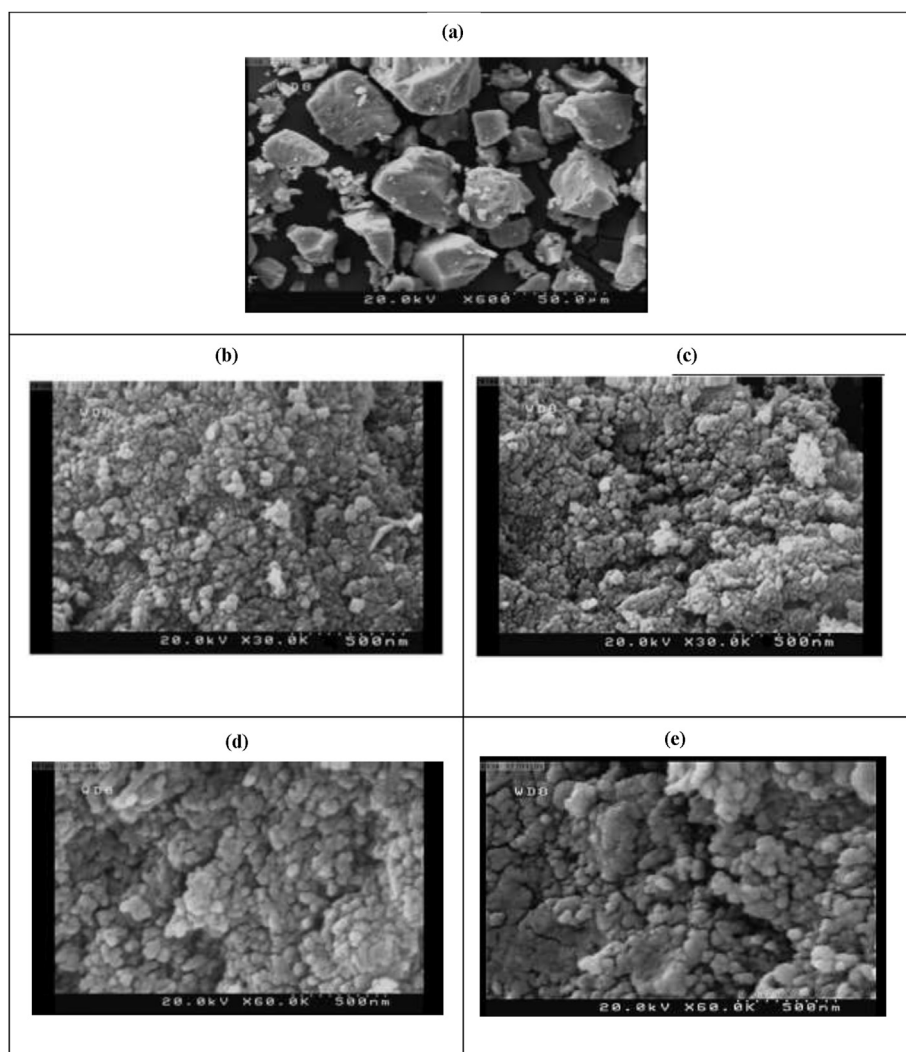
Figure 7. SEM images of samples (a) the original Pc-G, (b) run 11, (c) run 12, (d) run 15 and (e) run 8.

XRD technique can be used to investigate the crystallinity of the specimen. Figure 5(a, b) show the XRD results of the unprocessed and GAS-processed Pc-G crystals. The crystal structure of the processed specimens was similar to the original specimen. However, the nanoparticles showed lower degrees of crystallinity than the unprocessed particles. In this respect, the reduced peak intensity in the XRD results of the G AS-processed specimens indicated a decline in the crystallinity.

DSC analysis was performed for thermal analysis of the processed and unprocessed particles. DSC test can be applied for detecting the crystal formation from the difference in the crystal melting point and latent heat of fusion and also, those of its constituents by the endotherm phase [65]. In fact, DSC analysis highlights the thermal behavior of the crystals in terms of the solid–liquid (fusion) and solid–solid (polymorphic transformation) transition curves [65]. Figure 6 shows the DSC thermograms of the original (unprocessed) and GAS-processed specimens. As shown in Figure 6 (a, b), melting points of the pure Pc-G and GAS-processed Pc-G were equal to 798.76 and 794.81 °C, respectively. Such a decline in the melting point of the nanoparticles can be explained by the enhanced heat transfer area and the reduced crystallinity. Also, the latent heat of fusion was at 37.85 J/gr for the unprocessed particles whereas it was at 36.88 J/gr for the processed particles. This reduction might be due to the lower size and amorphous structure of the particles.

As suggested by the SEM imaging of the particles (Figure 7(a–e)), a significant reduction was observed in the size along with a variation in the morphological features of the GAS-processed particles. Furthermore, the unprocessed specimens exhibited the irregular and angular morphologies while, the GAS-processed particles were semispherical particles with the enhanced distribution. The SEM results showed a good consistency with the DLS tests. According to the DLS analysis, the particle size of the processed specimens varied in the range of 27.1–233.6 nm exhibiting finer particles with narrower distribution compared to the original ones. Figure 8 (a–d) present the DLS graphs.

4.4. Thermodynamic modeling and molar volume expansion

Modeling of the binary and ternary systems composed of Pc-G, DMSO, and CO_2 was conducted using the Peng-Robinson equation of state (PR EoS) at three different temperatures (308, 318, and 328 K). For this purpose, the molar volume expansion was studied in the expanded liquid phase. Table 4 summarizes the critical features as well as the acentric factors of Pc-G, DMSO, and CO_2. Moreover, Table 5 presents the physical properties of the Pc-G in Eq. (18). Table 6 also shows the values of binary interaction parameters. Peng-Robinson EoS was considered for estimation of the overall volume expansion in the equilibrated liquid phase of binary (DMSO–SC-CO_2) and ternary (DMSO – Pc-G – SC-CO_2) systems. In this context, calculation of the operating conditions is essential for solute precipitation in the GAS process. A plot of the relative molar volume as a function of pressure could be used to determine the minimum operation
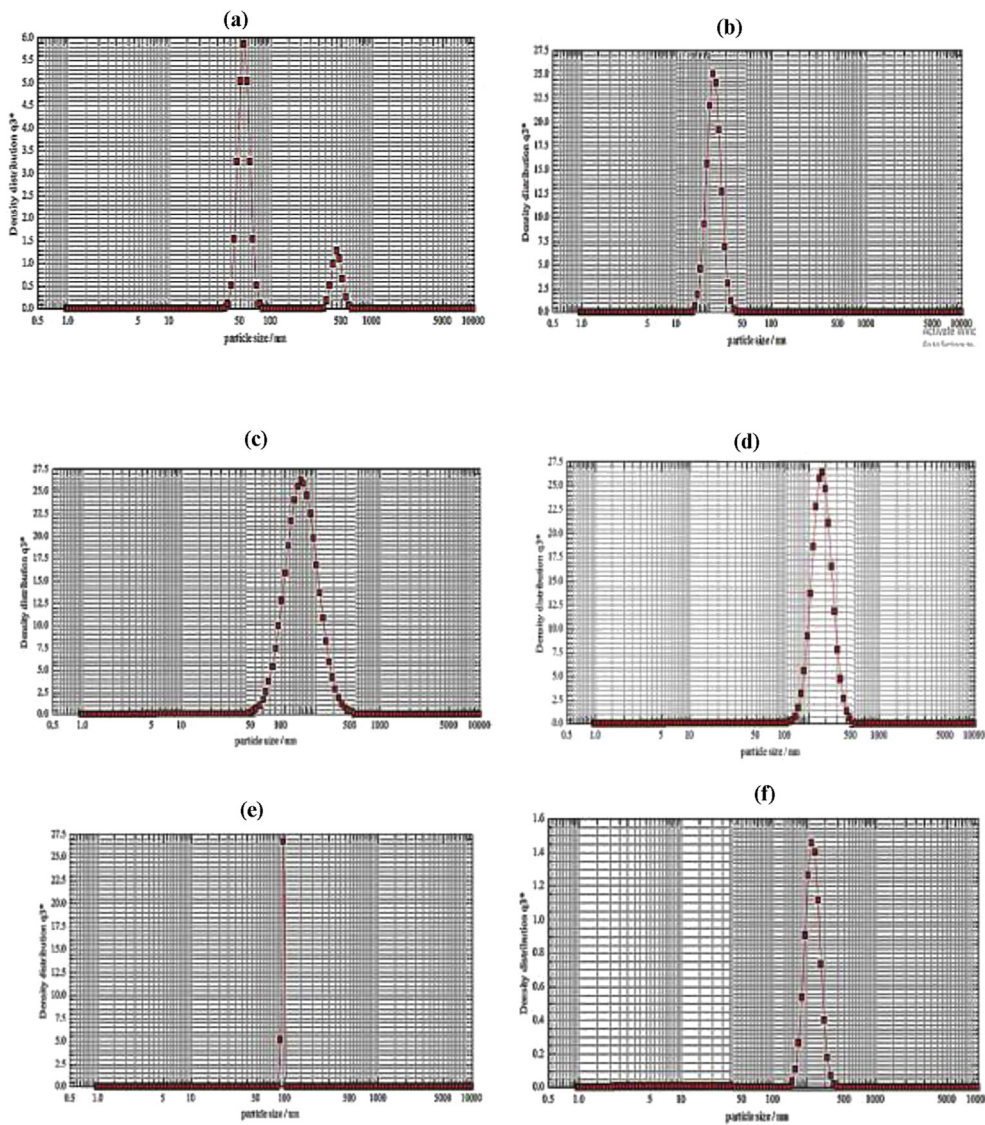
Figure 8. DLS graphs obtained under various GAS process conditions (based on Table 2): (a) run 1, (b) run 4, (c) run 7, (d) run 8, (e) run 12 and (f) run 15.

Table 4. Critical properties and acentric factor of substances.

Substance	Tc (K)	Pc (MPa)	ω	Ref.
CO_2	304.13	7.38	0.22	[60]
DMSO	706.9	5.85	0.45	[60]
Pc-G	1165.84	1.233	2.04	this work

Table 5. Thermophysical properties of pure component.

Component	T_b (K)	T_m (K)	v_s ($cm^3.mol^{-1}$)	MW ($g.mol^{-1}$)	P_{tp} (MPa)	v_{tp} ($cm^3.mol^{-1}$)	ΔH_{tp} ($kJ.g^{-1}$)
Pc-G	1009.82	798.76	350.5	1127.154	7.15×10^{-7}	350.4	26.499

Table 6. Binary interaction parameters for various conditions.

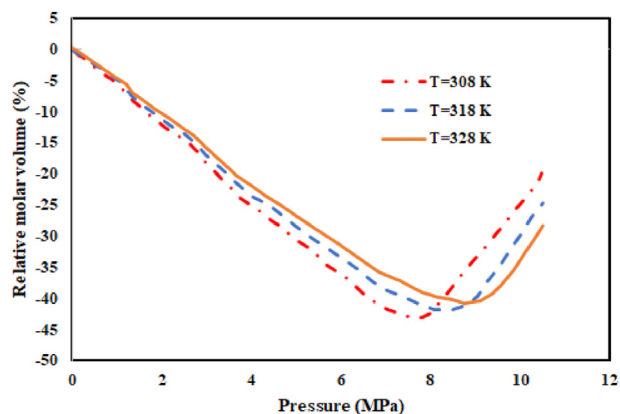| Temperature	k_{ij}	l_{ij}
T = 308 K	0.25	0.08
T = 318 K	0.14	-0.05
T = 328 K	0.04	-0.16

Figure 9. The molar volume expansion of the binary system CO_2 + DMSO at T = (308, 318 and 328 K) computed by PR EoS.
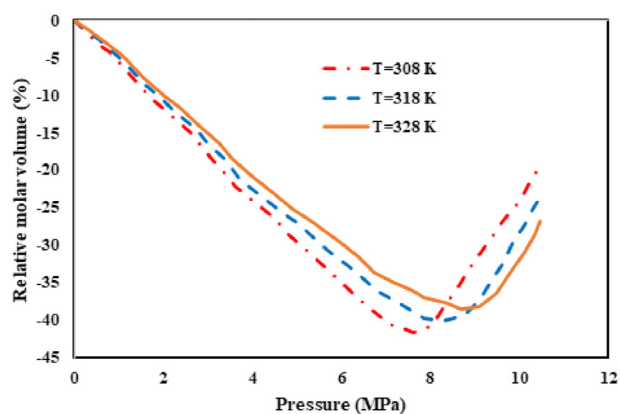

Figure 10. The molar volume expansion of the ternary system CO_2 + DMSO + Pc-G at T= (308, 318 and 328 K) computed by PR EoS.

Figure 11. Mole fraction of components in the liquid phase in the ternary system of Pc-G- CO_2- DMSO at a) 308 K, b) 318 K and c) 328 K calculated by the thermodynamic model.

pressure for different temperatures (Figures 9 and 10). Accordingly, in this study, the operation pressure exceeded P_{min}.

As demonstrated in Figure 10, for the ternary system of CO_2–DMSO–Pc-G, the minimum pressure showed an enhancement with the increase in the temperature. A rise in the temperature also augmented the solubility of the Pc-G in the DMSO causing an enhancement in the minimum pressure required for particle precipitation. This phenomenon can be also seen in Figure 11(a–c).

Figure 11(a–c) present the mole fractions for each component predicted by the PR EoS. The lowest Pc-G concentration in the liquid phase was determined at the pressure similar to that of volume expansion curve. The results presented in Figures 9 and 10 could be confirmed by those in Figure 11(a–c). Under the mentioned conditions, most of the Pc-G content was precipitated. Relative variation in the molar volume exhibited an enhancement by elevating the CO_2 liquid mole fraction. At the beginning of the experiment, the dissolved Pc-G- DMSO solution was introduced into the cell. Upon addition of CO_2, it was also dissolved in the DMSO. This resulted in the precipitation of Pc-G and hence, a decline in its mole fraction in the liquid phase. These findings can be helpful in the selection of real experimental conditions.

The calculated P_{min} values of the ternary system were equal to 7.87, 8.48, and 8.95 MPa at temperatures of 308, 318, and 328 K, respectively. As demonstrated, the value of P_{min} for a binary system was less than that of the ternary system, at a fixed temperature.

Finally, the mole fractions of solid (pigment Pc-G) were calculated by the model. The results regarding the minimum value of pigment concentration in the liquid phase were obtained at the pressure similar to
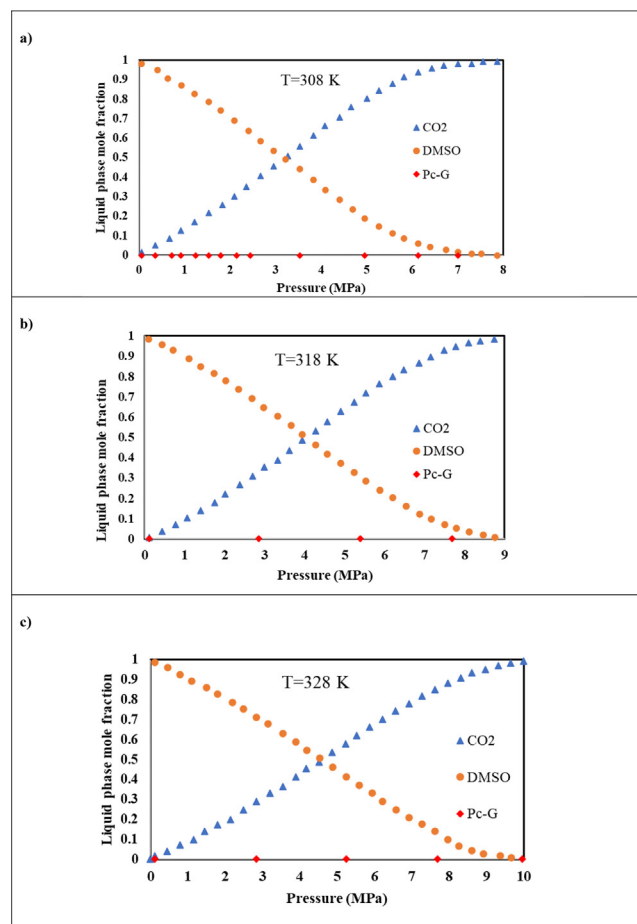
that of the volume expansion curve. The process pressure should be above P_{min}. Operation at the aforementioned pressure and temperature assured the precipitation of most volume of the pigment. With the increase in the pressure, a sharp decrease was observed in the Pc-G solubility in the liquid phase. The minimum solute solubility in the liquid phase was found at the pressures above P_{min}. An increase in the relative variation of molar volume occurred with an increase in the liquid mole fraction of CO_2. At the beginning of the experiment, the Pc-G-DMSO solution was placed in the precipitator. The CO_2 was added to this solution and consequently, it was dissolved in the DMSO. The pigment was precipitated and its mole fraction was decreased in the liquid phase. These results helped to select the actual experimental operating conditions and kinetic modeling. However, the amount of minimum pressure (Pmin) was found to increase by increasing the temperature, which can be due to the increased pigment solubility as a result of the increase in the temperature.

5. Conclusion

Production of Pc-G nanoparticles by gas antisolvent (GAS) method was addressed in the current study, for the first time. The use of smaller particles can increase the solubility of the pigments with low water-solubility. The impacts of different factors (i.e. pressure, temperature, and solute concentration) on the size and morphology of the produced Pc-G particles were investigated. Based on the Box–Behnken experimental design (BBD), an increase in the temperature and/or solute

concentration enhanced the particles size; while the pressure elevation led to the formation of smaller particles. The size of GAS-produced Pc-G nanoparticles varied from 27.1 to 233.6 nm. The GAS-precipitated particles had almost spherical shapes. Furthermore, the Peng Robinson (PR) EoS was used to investigate the phase equilibrium behavior (fluid phases) of the binary (CO_2– Pc-G) and ternary (CO_2–Pc-G and DMSO) systems. Additionally, an independent equation was utilized for the solid phase. The liquid phase volume expansion as well as the relative molar volume was also determined. Finally, the results indicated that the minimum pressure could be enhanced by the temperature elevation.

Declarations

Author contribution statement

Gholamhossein Sodeifian: Conceived and designed the experiments; Analyzed and interpreted the data; Wrote the paper.

Nedasadat Saadati ardestani: Performed the experiments; Contributed reagents, materials, analysis tools or data; Wrote the paper.

Seyed Ali Sajadian: Conceived and designed the experiments; Contributed reagents, materials, analysis tools or data.

Funding statement

Competing interest statement

The authors declare no conflict of interest.

Additional information

No additional information is available for this paper.

References

[1] G. Sodeifian, N.S. Ardestani, S.A. Sajadian, K. Moghadamian, Properties of Portulaca oleracea seed oil via supercritical fluid extraction: experimental and optimization, J. Supercrit. Fluids 135 (2018) 34–44.

[2] G. Sodeifian, S.A. Sajadian, N.S. Ardestani, Experimental optimization and mathematical modeling of the supercritical fluid extraction of essential oil from Eryngium billardieri: application of simulated annealing (SA) algorithm, J. Supercrit. Fluids 127 (2017) 146–157.

[3] M. McHugh, V. Krukonis, Supercritical Fluid Extraction: Principles and Practice, Elsevier, 2013.

[4] G. Brunner, Applications of supercritical fluids, Annu. Rev. Chem. Biomol. Eng. 1 (2010) 321–342.

[5] M. Herrero, J.A. Mendiola, A. Cifuentes, E. Ibáñez, Supercritical fluid extraction: recent advances and applications, J. Chromatogr. A 1217 (2010) 2495–2511.

[6] Ž. Knez, E. Markočič, M. Leitgeb, M. Primožič, M.K. Hrnčič, M. Škerget, Industrial applications of supercritical fluids: a review, Energy 77 (2014) 235–243.

[7] N. Esfandiari, S.M. Ghoreishi, Optimal thermodynamic conditions for ternary system (CO2, DMSO, ampicillin) in supercritical CO_2 antisolvent process, J. Taiwan Inst. Chem. Eng. 50 (2015) 31–36.

[8] A. Jouyban, M. Khoubnasabjafari, W. Acree Jr., Mathematical representation of solute solubility in binary mixture of supercritical fluids by the Jouyban-Acree model, Die Pharmazie Int. J. Pharmaceut. Sci. 60 (2005) 527–529.

[9] G. Sodeifian, S.A. Sajadian, N.S. Ardestani, Determination of solubility of Aprepitant (an antiemetic drug for chemotherapy) in supercritical carbon dioxide: empirical and thermodynamic models, J. Supercrit. Fluids 128 (2017) 102–111.

[10] G. Sodeifian, N.S. Ardestani, S.A. Sajadian, H.S. Panah, Experimental Measurements and Thermodynamic Modeling of Coumarin-7 Solid Solubility in Supercritical Carbon Dioxide: Production of Nanoparticles via RESS Method, Fluid Phase Equilibria, 2018, pp. 122–143.

[11] J. Del Valle, T. Rogalinski, C. Zetzl, G. Brunner, Extraction of boldo (Peumus boldus M.) leaves with supercritical CO_2 and hot pressurized water, Food Res. Int. 38 (2005) 203–213.

[12] B.A.S. Machado, C.G. Pereira, S.B. Nunes, F.F. Padilha, M.A. Umsza-Guez, Supercritical fluid extraction using CO2: main applications and future perspectives, Separ. Sci. Technol. 48 (2013) 2741–2760.

[13] K. Pitchaiah, N. Lamba, J. Deepitha, P. Mohapatra, G. Madras, N. Sivaraman, Experimental measurements and correlation of the solubility of N, N-dialkylamides in supercritical carbon dioxide, J. Supercrit. Fluids 143 (2019) 162–170.

[14] R. Melgosa, M.T. Sanz, Ó. Benito-Román, A.E. Illera, S. Beltrán, Supercritical CO_2 assisted synthesis and concentration of monoacylglycerides rich in omega-3 polyunsaturated fatty acids, J. CO_2 Util. 31 (2019) 65–74.

[15] R. Monteagudo-Olivan, M.J. Cocero, J. Coronas, S. Rodríguez-Rojo, Supercritical CO2 encapsulation of bioactive molecules in carboxylate based MOFs, J. CO_2 Util. 30 (2019) 38–47.

[16] K. Byrappa, S. Ohara, T. Adschiri, Nanoparticles synthesis using supercritical fluid technology–towards biomedical applications, Adv. Drug Deliv. Rev. 60 (2008) 299–327.

[17] A. Martín, M.J. Cocero, Micronization processes with supercritical fluids: fundamentals and mechanisms, Adv. Drug Deliv. Rev. 60 (2008) 339–350.

[18] N. Esfandiari, Production of micro and nano particles of pharmaceutical by supercritical carbon dioxide, J. Supercrit. Fluids 100 (2015) 129–141.

[19] P. Kalantarian, A.R. Najafabadi, I. Haririan, A. Vatanara, Y. Yamini, M. Darabi, K. Gilani, Preparation of 5-fluorouracil nanoparticles by supercritical antisolvents for pulmonary delivery, Int. J. Nanomed. 5 (2010) 763.

[20] M. Müller, U. Meier, A. Kessler, M. Mazzotti, Experimental study of the effect of process parameters in the recrystallization of an organic compound using compressed carbon dioxide as antisolvent, Ind. Eng. Chem. Res. 39 (2000) 2260–2268.

[21] D. Jafari, I. Yarnezhad, S.M. Nowee, S.H.N. Baghban, Gas-antisolvent (GAS) crystallization of aspirin using supercritical carbon dioxide: experimental study and characterization, Ind. Eng. Chem. Res. 54 (2015) 3685–3696.

[22] Y. Bakhbakhi, S. Rohani, P.A. Charpentier, Micronization of phenanthrene using the gas antisolvent process. 1. Experimental study and use of FTIR, Ind. Eng. Chem. Res. 44 (2005) 7337–7344.

[23] G. Sodeifian, S.A. Sajadian, Solubility measurement and preparation of nanoparticles of an anticancer drug (Letrozole) using rapid expansion of supercritical solutions with solid cosolvent (RESS-SC), J. Supercrit. Fluids 133 (2018) 239–252.

[24] M.J. Cocero, A. Martin, Precipitation processes with supercritical fluids: patents review, Recent Pat. Eng. 2 (2008) 9–20.

[25] D.W. Matson, R.C. Petersen, R.D. Smith, Production of powders and films by the rapid expansion of supercritical solutions, J. Mater. Sci. 22 (1987) 1919–1928.

[26] R.S. Mohamed, P.G. Debenedetti, R.K. Prud'homme, Effects of process conditions on crystals obtained from supercritical mixtures, AIChE J. 35 (1989) 325–328.

[27] L. Songtipya, A. Sane, Effect of concentration and degree of saturation on co-precipitation of catechin and poly (l-lactide) by the RESOLV process, J. Supercrit. Fluids 75 (2013) 72–80.

[28] K. Mishima, K. Matsuyama, D. Tanabe, S. Yamauchi, T.J. Young, K.P. Johnston, Microencapsulation of proteins by rapid expansion of supercritical solution with a nonsolvent, AIChE J. 46 (2000) 857–865.

[29] J.T. Essel, A.C. Cortopassi, K.K. Kuo, Synthesis and characterization of coated energetic materials using a RESS-N system, Int. J. Energy Mater. Chem. Propuls. 9 (2010) 112–1121.

[30] N. Esfandiari, S.M. Ghoreishi, Kinetics modeling of ampicillin nanoparticles synthesis via supercritical gas antisolvent process, J. Supercrit. Fluids 81 (2013) 119–127.

[31] N. Esfandiari, S.M. Ghoreishi, Ampicillin nanoparticles production via supercritical CO 2 gas antisolvent process, Am. Assoc. Pharmaceut. Sci. 16 (2015) 1263–1269.

[32] E. Reverchon, I. De Marco, G. Della Porta, Rifampicin microparticles production by supercritical antisolvent precipitation, Int. J. Pharm. 243 (2002) 83–91.

[33] R. Thiering, F. Dehghani, N.R. Foster, Current issues relating to anti-solvent micronisation techniques and their extension to industrial scales, J. Supercrit. Fluids 21 (2001) 159–177.

[34] E. Torino, I. De Marco, E. Reverchon, Organic nanoparticles recovery in supercritical antisolvent precipitation, J. Supercrit. Fluids 55 (2010) 300–306.

[35] R.L. Matos, T. Lu, V. Prosapio, C. McConville, G. Leeke, A. Ingram, Coprecipitation of curcumin/PVP with enhanced dissolution properties by the supercritical antisolvent process, J. CO_2 Util. 30 (2019) 48–62.

[36] P. Franco, E. Reverchon, I. De Marco, Zein/diclofenac sodium coprecipitation at micrometric and nanometric range by supercritical antisolvent processing, J. CO_2 Util. 27 (2018) 366–373.

[37] E. Reverchon, G. Della Porta, Micronization of antibiotics by supercritical assisted atomization, J. Supercrit. Fluids 26 (2003) 243–252.

[38] K. Moribe, M. Fukino, Y. Tozuka, K. Higashi, K. Yamamoto, Prednisolone multicomponent nanoparticle preparation by aerosol solvent extraction system, Int. J. Pharm. 380 (2009) 201–205.

[39] J. Jia, J. Wang, K. Zhang, D. Zhou, F. Ge, Y. Zhao, Aescin nanoparticles prepared using SEDS: composition stability and dissolution enhancement, J. Supercrit. Fluids 130 (2017) 267–272.

[40] D.J. Jarmer, C.S. Lengsfeld, T.W. Randolph, Manipulation of particle size distribution of poly (L-lactic acid) nanoparticles with a jet-swirl nozzle during precipitation with a compressed antisolvent, J. Supercrit. Fluids 27 (2003) 317–336.

[41] W. Chen, X. Hu, Y. Hong, Y. Su, H. Wang, J. Li, Ibuprofen nanoparticles prepared by a PGSS™-based method, Powder Technol. 245 (2013) 241–250.

[42] E. Weidner, High pressure micronization for food applications, J. Supercrit. Fluids 47 (2009) 556–565.

[43] S. Varona, S. Kareth, Á. Martín, M.J. Cocero, Formulation of lavandin essential oil with biopolymers by PGSS for application as biocide in ecological agriculture, J. Supercrit. Fluids 54 (2010) 369–377.

[44] A.V. Nunes, C.M. Duarte, Dense CO_2 as a solute, co-solute or co-solvent in particle formation processes: a review, Materials 4 (2011) 2017–2041.

[45] A. Tabernero, E.M.M. del Valle, M.A. Galán, Supercritical fluids for pharmaceutical particle engineering: methods, basic fundamentals and modelling, Chem. Eng. Process Process Intensification 60 (2012) 9–25.

[46] E. Reverchon, R. Adami, S. Cardea, G. Della Porta, Supercritical fluids processing of polymers for pharmaceutical and medical applications, J. Supercrit. Fluids 47 (2009) 484–492.

[47] S.-D. Yeo, E. Kiran, Formation of polymer particles with supercritical fluids: a review, J. Supercrit. Fluids 34 (2005) 287–308.

[48] G. Sodeifian, S.A. Sajadian, Utilization of ultrasonic-assisted RESOLV (US-RESOLV) with polymeric stabilizers for production of amiodarone hydrochloride nanoparticles: optimization of the process parameters, Chem. Eng. Res. Des. 142 (2019) 268–284.

[49] G. Sodeifian, S.A. Sajadian, N.S. Ardestani, F. Razmimanesh, Production of Loratadine drug nanoparticles using ultrasonic-assisted Rapid expansion of supercritical solution into aqueous solution (US-RESSAS), J. Supercrit. Fluids (2018).

[50] M. Gordillo, C. Pereyra, E.M. de la Ossa, Solubility estimations for Disperse Blue 14 in supercritical carbon dioxide, Dyes Pigments 67 (2005) 167–173.

[51] G.D. Bothun, K.L. White, B.L. Knutson, Gas antisolvent fractionation of semicrystalline and amorphous poly (lactic acid) using compressed CO2, Polymer 43 (2002) 4445–4452.

[52] M. Cocero, S. Ferrero, Crystallization of β-carotene by a GAS process in batch effect of operating conditions, J. Supercrit. Fluids 22 (2002) 237–245.

[53] J. De la Fuente Badilla, C. Peters, J. de Swaan Arons, Volume expansion in relation to the gas–antisolvent process, J. Supercrit. Fluids 17 (2000) 13–23.

[54] H. Pahlavanzadeh, H. Bakhshi, H.A. Shirazizadeh, Experimental measurement and phase equilibria calculation for ternary systems of carbon dioxide+ toluene+ naphthalene and carbon dioxide+ ethanol+ acridine, applicable for fine particle production in GAS process, Thermochim. Acta 638 (2016) 69–79.

[55] C. Juan, A. Shariati, C.J. Peters, On the selection of optimum thermodynamic conditions for the GAS process, J. Supercrit. Fluids 32 (2004) 55–61.

[56] A. Shariati, C. Peters, Measurements and modeling of the phase behavior of ternary systems of interest for the GAS process: I. The system carbon dioxide+ 1-propanol+ salicylic acid, J. Supercrit. Fluids 23 (2002) 195–208.

[57] D. Jafari, S. Nowee, S. Noie, A kinetic modeling of particle formation by gas antisolvent process: precipitation of aspirin, J. Dispersion Sci. Technol. 38 (2017) 677–685.

[58] T. Basova, P. Semyannikov, V. Plyashkevich, A. Hassan, I. Igumenov, Volatile phthalocyanines: vapor pressure and thermodynamics, Crit. Rev. Solid State Mater. Sci. 34 (2009) 180–189.

[59] P. Semyannikov, T. Basova, S. Trubin, E. Kol'tsov, I. Igumenov, Vapor pressure measurements and thermodynamics of some volatile phthalocyanines, J. Porphyr. Phthalocyanines 10 (2006) 1034–1039.

[60] G. Sodeifian, N.S. Ardestani, S.A. Sajadian, Solubility measurement of a pigment (Phthalocyanine green) in supercritical carbon dioxide: experimental correlations and thermodynamic modeling, Fluid Phase Equil. 494 (2019) 61–73.

[61] N. Tafreshi, S. Sharifnia, S.M. Dehaghi, Box–Behnken experimental design for optimization of ammonia photocatalytic degradation by ZnO/Oak charcoal composite, Process Saf. Environ. Protect. 106 (2017) 203–210.

[62] A. Niazi, N. Khorshidi, P. Ghaemmaghami, Microwave-assisted of dispersive liquid–liquid microextraction and spectrophotometric determination of uranium after optimization based on Box–Behnken design and chemometrics methods, Spectrochim. Acta Part A Mol. Biomol. Spectrosc. 135 (2015) 69–75.

[63] K. Chen, X. Zhang, J. Pan, W. Zhang, W. Yin, Gas antisolvent precipitation of Ginkgo ginkgolides with supercritical CO2, Powder Technol. 152 (2005) 127–132.

[64] S.-D. Yeo, S.-D. Yeo, Recrystallization of caffeine using gas antisolvent process, J. Supercrit. Fluids 47 (2008) 85–92.

[65] N. Wichianphong, M. Charoenchaitrakool, Application of Box–Behnken design for processing of mefenamic acid–paracetamol cocrystals using gas anti-solvent (GAS) process, J. CO2 Util. 26 (2018) 212–220.

[66] K. Zhao, Y. Cheng, H. Liu, C. Yang, L. Qiu, G. Zeng, H. He, Extractive desulfurization of dibenzothiophene by a mixed extractant of N, N-dimethylacetamide, N, N-dimethylformamide and tetramethylene sulfone: optimization by Box–Behnken design, RSC Adv. 5 (2015) 66013–66023.

[67] M. Mourabet, A. El Rhilassi, H. El Boujaady, M. Bennani-Ziatni, A. Taitai, Use of response surface methodology for optimization of fluoride adsorption in an aqueous solution by Brushite, Arab. J. Chem. 10 (2017) S3292–S3302.

[68] N. Sathyamoorthy, D. Magharla, P. Chintamaneni, S. Vankayalu, Optimization of paclitaxel loaded poly (ε-caprolactone) nanoparticles using Box Behnken design, Beni-Suef Univ. J. Basic Appl. Sci. 6 (2017) 362–373.

[69] D.-Y. Peng, D.B. Robinson, A new two-constant equation of state, Ind. Eng. Chem. Fundam. 15 (1976) 59–64.

[70] R.C. Reid, J.M. Prausnitz, B.E. Poling, The Properties of Gases and Liquids, 1987.

[71] Y. Bakhbakhi, P.A. Charpentier, S. Rohani, Experimental study of the GAS process for producing microparticles of beclomethasone-17, 21-dipropionate suitable for pulmonary delivery, Int. J. Pharm. 309 (2006) 71–80.

[72] S.-J. Kim, B.-M. Lee, B.-C. Lee, H.-S. Kim, H. Kim, Y.-W. Lee, Recrystallization of cyclotetramethylenetetranitramine (HMX) using gas anti-solvent (GAS) process, J. Supercrit. Fluids 59 (2011) 108–116.

[73] A. Hou, J. Dai, The crystal morphology of CI Disperse Blue 79 in supercritical carbon dioxide, Dyes Pigments 82 (2009) 71–75.

[74] D. Tuma, G.M. Schneider, High-pressure solubility of disperse dyes in near-and supercritical fluids: measurements up to 100 MPa by a static method, J. Supercrit. Fluids 13 (1998) 37–42.

[75] R. Ion, M. Ion, V. Niculescu, I. Dumitriu, R. Fierascu, G. Florea, C. Bercu, S. Serban, Spectral analysis of original and restaurated ancient paper from Romanian gospel, Rom. J. Phys. 53 (2008) 781–791.

[76] A. Verma, S. Saxena, G. Saini, V. Gaur, V. Jain, Hydrogen peroxide vapor sensor using metal-phthalocyanine functionalized carbon nanotubes, Thin Solid Films 519 (2011) 8144–8148.

[77] J. Wang, Y.q. Feng, J.y. Xie, G. Li, X.g. Li, Dispersion of phthalocyanine green G in nonaqueous medium using hyperdispersants and application in E-ink, J. Dispersion Sci. Technol. 27 (2006) 975–981.